AIAA 2003-0309

Large-Eddy Simulation of Pollutant Emission in a DOE-HAT Combustor

G. Eggenspieler and S. Menon,
School of Aerospace Engineering
Georgia Institute of Technology
Atlanta, Georgia 30332

41st Aerospace Sciences Meeting and Exhibit
January 6–9, 2003 / Reno, NV

Large-Eddy Simulation of Pollutant Emission in a DOE-HAT Combustor

G. Eggenspieler* and S. Menon†
School of Aerospace Engineering
Georgia Institute of Technology
Atlanta, Georgia 30332

Large-eddy simulation (LES) of turbulent premixed reacting flow in a DOE-HAT gas turbine combustor has been carried out to evaluate the use of LES to study combustion dynamics and to predict pollutant emission as lean-blow out (LBO) is approached. A localized dynamic model for the subgrid turbulent kinetic energy is used to close the subgrid stresses and heat flux in the LES equations, and a thin-flame turbulent propagation model is combined with a mixture fraction based flamelet library to predict the turbulence-chemistry interactions. Production of pollutants such as oxides of nitrogen (NO_x) and carbon monoxide (CO) are predicted using this model and compared to experimental data. Excellent agreement is obtained for CO and NO_x emission as a function of equivalence ratio and the simulations predict the observed increase in CO emission as LBO is approached. Simulations also show that the dynamical (unsteady) interactions increase in intensity as LBO is approached.

1 Introduction

Recent more stringent emission regulations have pushed for the development of more fuel efficient and low-NO_x gas turbine systems. However, design studies of new devices will require accurate prediction of emissions (CO, NO and UHC) as a function of the operating conditions. Recent measurements in a full-scale combustor (denoted DOE-HAT, hereafter)[1] showed that, as the equivalence ratio is decreased, the CO emission first decreases and then, suddenly increases exponentially. This phenomenon (which is also observed in many other liquid- and gaseous-fueled gas turbine combustors) can (in some cases) be followed by, or related, to combustion instability during which the flame undergoes rapid oscillations and eventual blows out. This process is often called the lean-blow out (LBO) and understanding and predicting this phenomenon is a major research issue. Past studies using RANS models[1] have been unable to capture this trend. More recently, a modified RANS approach using a flamelet model has been carried out at GEAEC[2,3,4] where good agreement with experimental data for the pollutant emission was demonstrated for a GE LM6000. However, the details of the combustion dynamics was not obtained since these studies did not account for the unsteady processes.

In the present effort, a new LES model is developed to study LBO in premixed combustion systems. The methodology follows closely the earlier study using the flamelet approach,[2,4] however, all closure issues are revisited within the LES subgrid formulation.

This paper is organized as follows. In the next section, the LES equations and the various closure issues and models are discussed in some detail for completeness. This is followed in Section 3 by the formulation of the flamelet approach as implemented here. In Section 4 the current numerical method is summarized and then, the results of the current study are described in Section 5.

2 LES Model Formulation

In this section, we describe the formulation of the LES model in some detail in order to establish the methodology used in the current study.

2.1 LES Equations

The governing equation of motion for an unsteady, compressible, reacting, multi-species fluid are the Navier-Stokes equations describing the conservation of mass, momentum, total energy and N-species. We employ the fully compressible version in this study since we are interested in the non-linear coupling between acoustic wave motion, vorticity dynamics and combustion heat release. In the LES methodology, the large scale motion is fully resolved on the computational grid using a time- and space-accurate scheme and only the small scales are modelled. The separation between the large (resolved) and the small (unresolved) scales is determined by the grid size ($\overline{\Delta}$). A Favre spatial top-hat filter (which is appropriate for the finite-volume scheme employed here) is employed to derive the LES equations.[5] Thus, any variable (f) is decomposed into a resolved quantity ($\widetilde{f}$) and a unresolved (quantity (f'') such that $f = \widetilde{f} + f''$. The resulting LEs equations are:[6]

*Student AIAA Member
†Professor, AIAA Associate Fellow

$$
\begin{cases}
\frac{\partial \overline{\rho}}{\partial t} + \frac{\partial \overline{\rho}\widetilde{u_i}}{\partial x_i} = 0 \\
\frac{\partial \overline{\rho}\widetilde{u_i}}{\partial t} + \frac{\partial}{\partial x_j}\Big[\overline{\rho}\widetilde{u_i}\widetilde{u_j} + \overline{p}\delta_{ij} - \overline{\tau_{ij}} + \tau_{ij}^{sgs}\Big] = 0 \\
\frac{\partial \overline{\rho}\widetilde{E}}{\partial t} + \frac{\partial}{\partial x_i}\Big[\Big(\overline{\rho}\widetilde{E} + \overline{p}\Big)\widetilde{u_i} + \\
\overline{q_i} - \widetilde{u_j}\overline{\tau_{ji}} + H_i^{sgs} + \sigma_i^{sgs}\Big] = 0 \\
\frac{\partial \overline{\rho}\widetilde{Y_m}}{\partial t} + \frac{\partial}{\partial x_j}\Big[\overline{\rho}\widetilde{Y_m}\widetilde{u_j} - \overline{\rho}\overline{D_m}\frac{\partial \widetilde{Y_m}}{\partial x_j} + \\
\Phi_{j,m}^{sgs} + \Theta_{jm}^{sgs}\Big] = \overline{\rho}\widetilde{\dot{w}}_m, m = 1, N
\end{cases}
$$

In the above equations, u_i is the i-th velocity component, ρ is the mass density, p is the pressure and $E = e + \frac{1}{2}(u_k^2 + k^{sgs})$ is the total energy. Here, e is the internal energy per unit mass computed as the sum of the sensible enthalpy and the chemical stored energy, and k^{sgs} is the subgrid kinetic energy (defined below). Also, q_i is the heat flux vector and τ_{ij} is the viscous stress tensor, given by $\tau_{ij} = \mu\Big(\partial u_i/\partial x_j + \partial u_j/\partial x_i\Big) - \frac{2}{3}\mu\Big(\partial u_k/\partial x_k\Big)\delta_{ij}$. Here, μ is the molecular viscosity coefficient which is determined using the Sutherland's law. Finally, Y_i is the species mass fraction and the molecular diffusion velocity $V_{j,m}$ is computed using the Fick's diffusion law with a constant diffusion coefficient (D_m): $V_{j,m} = -D_m\Big(\partial Y_m/\partial x_j\Big)$.

In the LES equations, all the above variables appear in their filtered form and many of these terms require closure. Some simplifications are required as well. For example, the filtered viscous shear stress ($\overline{\tau_{ij}}$) and heat flux ($\overline{q_i}$) are approximated using the filtered velocity and temperature . The subgrid terms in the equations represent the effect of the unresolved motion on the resolved field and are: τ_{ij}^{sgs}, H_i^{sgs}, σ_i^{sgs}, $\Phi_{j,m}^{sgs}$ and Θ_{jm}^{sgs}, and are respectively, the subgrid shear stress, subgrid heat flux, subgrid viscous stress, subgrid mass flux and subgrid diffusive mass flux. These terms are defined as follows:

$$
\begin{cases}
\tau_{ij}^{sgs} = \overline{\rho}\Big[\widetilde{u_i u_j} - \widetilde{u_i}\widetilde{u_j}\Big] \\
H_i^{sgs} = \overline{\rho}\Big[\widetilde{E u_i} - \widetilde{E}\widetilde{u_i}\Big] + \Big[\overline{p u_i} - \overline{p}\widetilde{u_i}\Big] \\
\sigma_i^{sgs} = \overline{u_j \tau_{ji}} - \widetilde{u_j}\overline{\tau_{ji}} \\
\Phi_{jm}^{sgs} = \overline{\rho}\Big[\widetilde{Y_m u_j} - \widetilde{Y_m}\widetilde{u_j}\Big] \\
\Theta_{jm}^{sgs} = \overline{\rho}\Big[Y_m\widetilde{V_{j,m}} - \widetilde{Y_m}\widetilde{V_{j,m}}\Big]
\end{cases} \quad (1)
$$

2.2 Subgrid Closure of the LES Equations

The closure of subgrid terms is a major area of research and many approaches have been proposed in the past. In general, since the small-scales primarily provide dissipation for the energy that cascades from the large scales through the inertial range, an eddy viscosity type subgrid model appears appropriate to model the subgrid stresses τ_{ij}^{sgs}, heat flux H_i^{sgs} and species flux Φ_{jm}^{sgs}. Assuming that an eddy viscosity ν_T can be prescribed, these subgrid fluxes can be approximated as:

$$
\begin{cases}
\tau_{ij}^{sgs} = -\nu_T\Big(\frac{\partial \widetilde{u_i}}{\partial x_j} + \frac{\partial \widetilde{u_j}}{\partial x_i}\Big) \\
H_i^{sgs} = -\nu_T\frac{\partial \widetilde{h}}{\partial x_i} \\
\Phi_{jm}^{sgs} = -D_T\Big(\frac{\partial \widetilde{Y_m}}{\partial x_j}\Big)
\end{cases} \quad (2)
$$

Here, $\widetilde{h}$ is the specific enthalpy and $D_T = \nu_T/Sc_t$ is the eddy diffusivity obtained in terms of the eddy viscosity and a turbulent Schmidt number Sc_t (assumed to be unity here). The subgrid diffusive mass flux (Θ_{jm}^{sgs}) is neglected in this study, and the closure for the subgrid viscous stress σ_i^{sgs} is described later. Finally, the closures of the filtered reaction rate $\widetilde{\dot{w}}_m$ is described in section 3.

To obtain the subgrid eddy viscosity ν_T, a characteristic length scale L^{sgs} and a characteristic velocity scale V^{sgs} for the unresolved scales of motion must be identified and prescribed, since the simplest model for ν_T is $\nu_T = C_\nu L^{sgs} V^{sgs}$. Here, C_ν is a coefficient of proportionality. In LES, the grid resolution $\overline{\Delta}$ is typically chosen as the characteristic length scale of the smallest resolved (or alternatively, the largest unresolved) eddy. However, it must be pointed out that numerically, the smallest eddy that can be resolved requires at least 3-4 grid points which implies that this choice is not necessarily correct but is within the range of acceptable length scales.

Subgrid models for eddy viscosity differ primarily in the prescription of the velocity scale, V^{sgs}. Earlier LES studies[7] used the resolved strain rate $\widetilde{S_{ij}} = \frac{1}{2}(\frac{\partial \widetilde{u_i}}{\partial x_j} + \frac{\partial u_j}{\partial x_i})$ and $\overline{\Delta}$ to obtain V^{sgs} such that $V^{sgs} = \overline{\Delta}S$ where $S = (\widetilde{S_{ij}}\widetilde{S_{ij}})^{1/2}$. With this closure, an algebraic eddy viscosity model is obtained and such a model has been employed in many simulations in the past. However, a limitation of this model is that the formal derivation of this eddy viscosity expression requires that production and dissipation of the turbulent kinetic energy must be in equilibrium. Since this requirement is only satisfied in the dissipation scales, proper application of the algebraic model requires that the entire inertial range is well resolved. This requirement is very severe for high-Re flows since the overall grid resolution required to meet this criteria can exceed available resource by a substantial amount. Therefore, for complex, high-Re flows an alternate choice, of the velocity scale is needed.

Here, we employ a transport model for the subgrid kinetic energy k^{sgs} to obtain V^{sgs}. This model is described below.

2.3 Subgrid Turbulent Kinetic Energy

A transport equation is formally derived for k^{sgs} and solved along with the rest of the LES equations. Since k^{sgs} evolves locally and temporally in the flow, the

equilibrium assumption is relaxed and now, the cutoff between the resolved and the unresolved scales can be in the inertial range instead of the dissipation range. Thus, a relatively coarse grid can be used to simulate LES of high Re flows. Past studies[8, 9, 6, 10] have demonstrated the ability and accuracy of this model.

The k^{sgs} transport model is given as:

$$\frac{\partial \overline{\rho} k^{sgs}}{\partial t} + \frac{\partial}{\partial x_i}\Big(\overline{\rho}\widetilde{u_i} k^{sgs}\Big) = P^{sgs} - D^{sgs} + \frac{\partial}{\partial x_i}\Big(\frac{\overline{\rho}\nu_T}{Pr_T}\frac{\partial k^{sgs}}{\partial x_i}\Big) \quad (3)$$

Here, the subgird kinetic energy is defined as $k^{sgs} = \frac{1}{2}\Big[\widetilde{u_k^2} - \widetilde{u_k}^2\Big]$, and Pr_T is a subgrid Prandtl number, assumed to be unity.

In the above equation, P^{sgs} and D^{sgs} represent respectively, the production and dissipation of the subgrid kinetic energy. These terms are modeled as follow:

$$P^{sgs} = -\tau_{ij}^{sgs}\frac{\partial \widetilde{u_i}}{\partial x_j} \quad (4)$$

$$D^{sgs} = C_\epsilon \overline{\rho}(k^{sgs})^{3/2}/\overline{\Delta} \quad (5)$$

The subgrid stress using k^{sgs} model is then obtained as:

$$\tau_{ij}^{sgs} = -2\overline{\rho}\nu_T\Big(\widetilde{S_{ij}} - \frac{1}{3}\widetilde{S_{kk}}\delta_{ij}\Big) + \frac{2}{3}\overline{\rho}k^{sgs}\delta_{ij} \quad (6)$$

where the subgrid eddy viscosity is given by

$$\nu_T = C_\nu (k^{sgs})^{1/2}\overline{\Delta} \quad (7)$$

In the above equation, two model coefficients C_ϵ and C_ν appear and they must be prescribed or obtained dynamically as a part of the solution. Earlier studies[9, 6, 10] established a localized dynamic scale-similarity approach that did not employ the Germano's identity. This approach resulted in a robust and stable approach for determining the model coefficients locally in the combustor without requiring any averaging or smoothing. In the present study, we employ constant values of $C_\nu = 0.067$ and $C_\epsilon = 0.916$ that were established earlier using theoretical and numerical studies of high-Re stagnation point premixed flames.[11, 12] Localized dynamic evaluation of the model coefficients will be considered in the near future but the results reported here are not expected to be very sensitive to this issue.

3 Combustion and Heat Release Models

A thin-flame propagation model is employed here to resolve the flame in the flamelet burning regime. In this regime, the flame thickness (δ_L) is smaller than the smallest length scale (Kolmogorov scale η) and the burning time scale (τ_c) is smaller than the characteristic flow time (τ_f). This is generally the case in gas turbine combustion chamber. In this case, the thin laminar flame is wrinkled by the turbulent eddies, thereby increasing the instantaneous flame surface and hence, the effective burning or consumption rate. However, since even the smallest eddy is larger than the flame thickness they cannot penetrate into the flame and thus, the local burning speed is still given by the laminar flame speed S_L. This approximation implies that classical methods to compute the laminar flame properties, such as the CHEMKIN program[13] can be used effectively.

It is worth noting that although flamelet burning is prevalent in gas turbine combustors, there are also local regimes where the turbulence levels are so high that the smallest eddy is smaller than the flame thickness. This regime of burning is called distributed reaction zone or thin reaction zone[14] and in this regime, the smaller eddies penetrate into the flame zone thereby, thickening the flame. However, past studies have shown that even in this regime, the reaction zone is very thin and hence, flamelet burning approximation can still be employed. Models that explicitly accounts for flame broadening effect in the thin-reaction zone regime have also been developed.[10]

Two features are unique to this approach. The flame propagation model is based on the G-equation approach used in LES studies[6, 10] and the turbulent burning speed is determined as a function of subgrid effects and laminar flamelet burning speed. The details of this approach is summarized below.

3.1 Flame Propagation

To track the flame without using finite-rate kinetics, a flame front tracking model is employed. In this approach, the flame front is tracked as a infinitely thin surface that is convected by the flow and also propagates normal to itself at a characteristic flame speed S_F. The governing equation for this progress variable is based on the G-equation model:

$$\frac{\partial \rho G}{\partial t} + \frac{\partial}{\partial x_i}\Big(\rho u_i G\Big) = -\rho S_F |\nabla G| \quad (8)$$

Here, G is a progress variable that has no physical meaning except that it is a level surface that resides between $G = 1$ representing premixed fuel and $G = 0$ representing the burnt products. In laminar flow, $S_F = S_L$ which is the laminar burning speed. This speed contains the effect of the entire thermo-chemical state of the fuel-air mixture. Thus, for a given equivalence ratio S_L is uniquely defined.

By filtering this equation using the LES filter described in Section 2.2 LES G-equation is obtained:

$$\frac{\partial \overline{\rho}\widetilde{G}}{\partial t} + \frac{\partial}{\partial x_i}\left(\overline{\rho}\widetilde{u}_i\widetilde{G}\right) = -\frac{\partial}{\partial x_i}\overline{\rho}\left(\widetilde{u_i G} - \widetilde{u}_i\widetilde{G}\right) - \overline{\rho S_F|\nabla G|} \tag{9}$$

The right hand side of Eqn. (9) needs to be modelled. The subgrid convection term is modelled using a gradient assumption that incorporates the effect of the curvature of the flame as:[14]

$$-\frac{\partial}{\partial x_i}\left(\widetilde{u_i G} - \widetilde{u}_i\widetilde{G}\right) = -\overline{\rho} D_T \widetilde{\kappa}|\nabla \widetilde{G}| \tag{10}$$

where $\widetilde{\kappa}$ is the flame curvature defined as:

$$\widetilde{\kappa} = \nabla \mathbf{n} \tag{11}$$

and

$$\mathbf{n} = -\frac{\nabla \widetilde{G}}{|\nabla \widetilde{G}|} \tag{12}$$

Here, $\mathbf{n}$ is the unit normal oriented in the direction of flame propagation. The flame front propagation term $\overline{\rho S_F|\nabla G|}$ is closed using a characteristic flame speed model. Thus, closed LES equation for the filtered progress variable G is:

$$\frac{\partial \overline{\rho}\widetilde{G}}{\partial t} + \frac{\partial}{\partial x_i}\left(\overline{\rho}\widetilde{u}_i\widetilde{G}\right) = -\overline{\rho} S_F|\nabla \widetilde{G}| - \overline{\rho} D_T \widetilde{\kappa}|\nabla \widetilde{G}| \tag{13}$$

Note that in the present implementation, the LES-resolved variable $\widetilde{G}$ can range from 0 to 1 and represents a measure of the flame brush thickness. This is in contrast to the original "laminar" interpretation of the G field where $G = 0$ denotes burned product and $G = 1$ denotes reactants and the flame is considered an infinitely thin interface between $G = 0$ and $G = 1$. In the LES implementation, the filtered $\widetilde{G}$ represents the resolved flame brush which is an average location of the instantaneous thin flames.

3.2 Turbulent Burning Speed

Although the laminar burning speed is well defined and can be determined using detailed chemical kinetics, in turbulent flow the flame is wrinkled by local fine-scale eddies and this results in an effective increase in burning speed or reactant consumption. Within the context of the thin-flame model, a turbulent flame speed S_T is assumed to exist with which the local flame surface (represented by $\widetilde{G}$) propagates into the reactant. Thus, $S_F = S_T$ in turbulent flow and typically, $S_T = S_T(u', S_L)$, where u' is subgrid turbulence intensity. Various models have been proposed but here we follow the model used in our earlier LES studies of gas turbine combustor flows.[6,10] This model is based on the Pocheau's model[15] and can be written as

$$\frac{S_T}{S_L} = \left(1 + \beta \frac{u'^{\alpha}}{S_L^{\alpha}}\right)^{\frac{1}{\alpha}} \tag{14}$$

where α=2 is chosen to conserve the energy and β is the minimum of $0.8165 * u'/S_L$ and 16.56. This minima is imposed such that S_T tends to zero when S_L tends to zero.

Proper estimate of the magnitude and proper resolution of the spatial structure of the subgrid u' are critical for accurate estimate of S_T using this model. Here, the k^{sgs} used in the subgrid closure for momentum transport can be used to obtain $u' = \left(\frac{2}{3}k^{sgs}\right)^{1/2}$. Note that, in contrast, an algebraic eddy viscosity closure does not provide a proper estimate for u'.

A localized dynamic model that extends S_T model to the thin-reaction zone is also available.[10] Studies have shown that this closure allows the study of gas turbine combustion over a wide range of operating conditions (i.e., flamelet and thin-reaction zone regimes) using the same flame propagation model. This is important since in real gas turbine combustors, both flamelet and distributed burning can spatially coexist due to variations in mixing and turbulent fluctuation. This is an issue that will be addressed in the future.

Although laminar flame speed is obtained from the CHEMKIN library as a function of mixture fraction (as described in the next section, additional effect of thermal expansion has to be included. If S_{L_u} is the laminar flame speed with respect to the unburnt gas, the effective laminar flame speed S_L is: $S_L = S_{L_u}\frac{\rho_u}{\rho}$ where ρ_u is the unburnt gas density and ρ is the actual gas density. With this definition, the final form of the turbulent burning speed is $S_F = S_T(S_L, u')\frac{\rho_u}{\rho}$.

3.3 Laminar Burning Speed

To obtain the laminar burning rate, S_L the detailed chemical kinetics occuring in the flame has to be properly estimated. Here, we employ a flamelet library approach since it is computationally efficient. In the flamelet library approach, the local chemical state is related to the mixture fraction $\widetilde{Z}$ which is obtained by the solution of a transport equation along with the LES equations. The influence of the subgrid turbulence upon the mixture fraction is included by solving another equation for the variance of the mixture fraction ($\widetilde{Z''^2}$). A simplified 1D problem is solved using detailed kinetics and the results such as the major species and the laminar burning rate S_L are tabulated as a function of $\widetilde{Z}$ and $\widetilde{Z''^2}$, and then retrieved during the actual calculation.

It is clear that this approach substantially reduces the total cost of the simulation since chemical species are not tracked for in the LES, and the stiffness of the chemical source terms is avoided. On the other hand, there are also some limitations. The flow must be such that a mixture fraction can be uniquely defined. Equal diffusivity for all species is implicitly assumed in the combustor flow field since the mixture fraction is the only unknown variable (note that, during the flamelet

library generation, detailed multi-component diffusion can be included but its effect on the actual flow field, and especially radicals cannot be included directly in the mixture fraction formulation). Additionally, the formation of the pollutant species also cannot be accounted by this method and requires new models, as described later.

The governing LES equation for the filtered mixture fraction used in this study is:

$$\frac{\partial \overline{\rho}\widetilde{Z}}{\partial t} + \frac{\partial}{\partial x_i}\left(\overline{\rho}\widetilde{u_i}\widetilde{Z}\right) = \frac{\partial}{\partial x_i}\left((D + D_T)\overline{\rho}\frac{\partial \widetilde{Z}}{\partial x_i}\right) \quad (15)$$

The equation for the variance of the mixture fraction is described by N. Peters[14] and the filtered LES equation for $\widetilde{Z''^2}$ has the following form:

$$\frac{\partial \bar{\rho}\widetilde{Z''^2}}{\partial t} + \frac{\partial}{\partial x_i}\left(\overline{\rho}\widetilde{u_i}\widetilde{Z''^2}\right) = \frac{\partial}{\partial x_i}\left(D_T\overline{\rho}\frac{\partial \widetilde{Z''^2}}{\partial x_i}\right) + 2\overline{\rho}D_T\left(\nabla\widetilde{Z}\right)^2 - 2\overline{\rho}\frac{\epsilon}{k^{sgs}}\widetilde{Z''^2} \quad (16)$$

In this closure, an eddy turbulent diffusivity closure is employed to close the convective subgrid flux. The closure for filtered scalar dissipation rate ($\widetilde{\chi}$) is an important issue. It represents the effect of subgrid turbulence on $\widetilde{Z}$ which tends to reduce the variance of mixture fraction, i.e., the mixing due to the unresolved eddies will tend to reduce fluctuations in the mixture fraction, thus decreasing the value of its variance. The scalar dissipation is:

$$\widetilde{\chi} = 2D|\ \widetilde{\nabla Z''}\ |^2 \quad (17)$$

and is modelled as:[14]

$$\widetilde{\chi} = 2\frac{\epsilon}{k^{sgs}}\widetilde{Z''^2} \quad (18)$$

The dissipation of the subgrid TKE ϵ in the above expression is directly related to the subgrid kinetic energy: $\epsilon = C_\epsilon(k^{sgs})^{3/2}/\overline{\Delta}$.

3.4 Heat release

With the flame location and the local flame speed determined, the effect of combustion heat release (and the associated volumetric expansion) on fluid dynamics is included in the LES model. The product temperature T_p is a function of $\widetilde{Z}$ and $\widetilde{Z''^2}$ and is computed during the flamelet library generation. The amount of chemical energy (E_c) that will be released during the chemical reaction is defined as:

$$E_c = C_p(T_p - T_{ref}) \quad (19)$$

If F_b is the fraction of burnt product, the amount of chemical energy released (E_r) is:

$$E_r = F_b C_p(T_p - T_{ref}) \quad (20)$$

The fraction of burnt product is directly related to the value of G such that: F_b=$(1 - \widetilde{G})$.

Note that the temperature obtained from flamelet library is not the temperature of the post flame region in the real flame zone since convective processes, viscous and pressure work effects are not included in the CHEMKIN calculation. However, this temperature allows us to compute the amount of chemical energy that will be released by the reactions in the flame zone.

It should be noted that this thin-flame model does not account for flame quenching and re-ignition. In a real gas turbine combustor, local flame quenching is known to occur prior to and during LBO. Therefore, prediction of the dynamics around the LBO limit has to include local flame quenching mechanism. This is currently under study but is not straightforward to implement within the G-equation approach.

3.5 LES Prediction of Pollutant Emission

In the present study, we are primarily interested in predicting CO, NO_x and UHC emission as a function of equivalence ratio. Here, UHC represent the unburnt fuel (CH_4) that is formed via quenching. The production of these pollutants occur due to a combined effect of chemical kinetics and turbulent fluid dynamical processes. The local (laminar) kinetic process can be obtained using the flamelet library model but its actual use in the LES filtered equations requires additional considerations which are discussed in the following sections. To track and predict these species we solve the LES filtered species equations for each of these species of the form:

$$\frac{\partial \overline{\rho}\widetilde{Y}_m}{\partial t} + \frac{\partial}{\partial x_j}\left[\overline{\rho}\widetilde{Y}_m\widetilde{u_j} - \overline{\rho}D_m\frac{\partial \widetilde{Y}_m}{\partial x_j} + \overline{\rho}(\widetilde{Y_m u_j} - \widetilde{Y}_m\widetilde{u_j})\right] = \overline{\rho}\widetilde{\dot{w}}_m \quad (21)$$

Two terms require closure: (i) the subgrid scalar flux $\Phi_{jm}^{sgs} = \overline{\rho}(\widetilde{Y_m u_j} - \widetilde{Y_m}\widetilde{u_j})$ and (ii) the production/destruction term $\overline{\rho}\widetilde{\dot{w}}_m$. In the following, we describe the closures employed for each of these terms for the pollutant species.

The subgrid scalar flux Φ_{jm}^{sgs} is closed using the gradient diffusion closure described earlier in Section 2.2. This closure is not considered very accurate since the subgrid scalar flux is a small-scale phenomenon and scalar mixing and diffusion occur in the small-scales. However, in a conventional LES, the small-scale mixing is not resolved and therefore, models are needed to close the governing equations. An alternate approach which simulates the scalar fluxes within the subgrid has been developed[11,12] but is not employed here.

In the following sections, we discuss the closure of the chemical source term $\overline{\rho}\widetilde{\dot{w}}_m$ for both CO and NO_x.

3.6 Carbon Monoxide (CO) Closure

CO is formed and/or destroyed by four major mechanisms. All of these mechanisms have to be properly modelled in the simulation, and therefore, are discussed in some detail. The four mechanisms (and the nomenclature used to identify them) are:

- Formation of CO at the flame front (subscript ff).
- Oxidation of CO in the post flame region (subscript ox)
- Dissociation of CO_2 (subscript dis)
- Formation of CO formation via oxidation of unburned CH_4 (subscript $oxuhc$)

The overall production/destruction rate of CO can then be written as:

$$\widetilde{\dot{w}}_{CO} = \widetilde{\dot{w}}_{CO,ff} + \widetilde{\dot{w}}_{CO,ox} + \widetilde{\dot{w}}_{CO,dis} + \widetilde{\dot{w}}_{CO,oxuhc} \quad (22)$$

In the following separate sections, we discuss the modelling of each of these production/destruction terms since they all impact the overall CO emission in gas turbine engines.

3.6.1 CO production at the flame front

Due to the presence of radicals in the flame front (especially O), a large amount of CO will be produced at the flame front. The CHEMKIN program (used in the flamelet library generation) allows us to determine the fraction of CO formed at the front flame ($Y_{CO,ff}$) as a function of the mixture fraction and the variance of the mixture fraction. The formation of CO at the flame front is therefore, treated as a jump relationship, i.e., CO is produced in proportion to the amount of fuel (represented using the $\widetilde{G}$ variable) is consumed.[3,4] Thus, the CO production at the flame front is modelled as:

$$\widetilde{\dot{w}}_{CO,ff} = S_F \mid \nabla \widetilde{G} \mid Y_{COff} \quad (23)$$

Typically, the front flame formation lies, in terms of mass fraction, between 1 and 3 percent.

It should be noted that the value Y_{COff} computed by CHEMKIN corresponds to the pollutant formation of a laminar non-stretched flame. In the flamelet assumption, the flame is wrinkled by turbulent eddies but cannot change the laminar flame structure. Therefore, turbulence has no direct effect on the pollutant emission from the local laminar flame.

The above assumption is not generally valid since flame stretch can modify the local laminar flame structure (in the thin-reaction zone regime) and this can impact the local CO formation at the flame front. However, at this time, this effect is neglected but will be revisited later.

3.6.2 CO oxidation in the post flame region

Once CO is formed, it will be oxidized into CO_2. The flamelet approach allows us to determine the oxidation time scale $\tau_{CO,ox}$ of CO as a function of $\widetilde{Z}$ and $\widetilde{Z''^2}$ using the CHEMKIN program. The rate of oxidation of CO is given as $\widetilde{\dot{w}}_{CO,ox} = -\tau_{CO,ox}\widetilde{Y}_{CO}$. Here, $\tau_{CO,ox}$ being given by the library. An optimally designed combustion chamber will ensure that the majority of CO formed at the flame front will be oxidized in the post flame region so that the CO mass fraction at the combustion chamber outlet will tend towards the equilibrium value.

The reaction rate of CO oxidation in the post flame region is independent of the subgrid turbulence since CHEMKIN does not take into account the influence of turbulence. This is a fairly good assumption since the level of turbulence is low in majority of post flame region since the increased temperature increases the viscous dissipation which in turn, reduces turbulent fluctuations.

3.6.3 CO formation via CO_2 dissociation

The equilibrium value is defined as the CO mass fraction reached when the rate of CO consumption by oxidation equals the rate of CO production via CO_2 dissociation. The mechanism considered here is:

$$CO_2 + O \rightleftharpoons CO + O_2 \quad (24)$$

The CHEMKIN program allows us to determine the CO mass fraction at equilibrium ($Y_{CO,eq}$). The rate of formation of CO via CO_2 dissociation is taken as:

$$\widetilde{\dot{w}}_{CO,eq} = (1 - \widetilde{G})\tau_{CO,ox}Y_{CO,eq} \quad (25)$$

Note that when $\widetilde{Y}_{CO} = Y_{CO,eq}$ then $\widetilde{\dot{w}}_{CO,eq} = \widetilde{\dot{w}}_{CO,ox}$, i.e., the rate of oxidation of CO equals the rate of formation of CO via CO_2 dissociation. This approach assumes that the dissociation of CO_2 occurs at an infinitely fast rate. Therefore, Eqn. (25) should not be seen as the rate of formation of CO via the dissociation of CO_2 but rather as a correction term allowing $\widetilde{Y}_{CO}$ to tend to $Y_{CO,eq}$.

3.6.4 CO formation via UHC oxidation

CO production also occurs due to the UHC in the flame and post flame zones. As stated above, UHC production was neglected because it is assumed that UHC is a negligible source of carbon monoxide. Thus:

$$\widetilde{\dot{w}}_{CO,oxuhc} = 0 \quad (26)$$

Thus, the LES form for the CO governing equation is:

$$\frac{\partial \overline{\rho}\widetilde{Y}_{CO}}{\partial t} + \frac{\partial}{\partial x_i}\left(\overline{\rho}\widetilde{u_i}\widetilde{Y}_{CO}\right) =$$

$$\frac{\partial}{\partial x_i}\Big((D+D_T)\overline{\rho}\frac{\partial \widetilde{Y}_{CO}}{\partial x_i}\Big) + \overline{\rho}\Big(S_F \mid \nabla \widetilde{G} \mid Y_{CO,ff} - \tau_{CO,ox}\widetilde{Y}_{CO} + (1-\widetilde{G})\tau_{CO,ox}Y_{CO,eq}\Big) \quad (27)$$

3.7 Oxides of Nitrogen (NO_x) Closure

Two mechanisms related to NO formation are taken into account in the present study. The first mechanism is the production of NO at the flame front (subscript ff) and the second one is the production of nitric monoxide due to the Zeldovich mechanism in the post flame region (subscript zel). The formation of NO at the flame front is also called prompt mechanism and the formation of NO in the post flame region is also called thermal NO. Thus, the reaction rate for NO can be written as:

$$\widetilde{\dot{w}}_{NO} = \widetilde{\dot{w}}_{NO,ff} + \widetilde{\dot{w}}_{NO,zel} \quad (28)$$

Due to the large amount of O radical in the flame region, NO is formed as the gases pass through the flame front. The amount of NO released at the flame front $Y_{NO,ff}$ is computed by CHEMKIN as a function of the mixture fraction and the variance of the mixture fraction. The rate of formation ($\widetilde{\dot{w}}_{NO,ff}$) is computed with the same method used for the rate of formation of CO. Thus,

$$\widetilde{\dot{w}}_{NO,ff} = S_F \mid \nabla \widetilde{G} \mid Y_{NO,ff} \quad (29)$$

The rate of formation of NO in the post flame region is computed using the Zeldovich mechanism under the quasi-steady assumption, i.e., the concentration of O and N radicals are assumed equal to the O and N equilibrium concentrations. The Zeldovich mechanism considered herein is:

$$\begin{aligned} N_2 + O &\rightleftharpoons NO + N \\ O_2 + N &\rightleftharpoons NO + O \end{aligned} \quad (30)$$

Under the quasi-steady assumption, where O, N, N_2 and O_2 mass fraction are considered to be constant, CHEMKIN can be used to compute the rate of formation of NO via this mechanism. This rate, $\dot{w}_{NO,zel_{CHEMKIN}}$ is a function of $\widetilde{Z}$ and $\widetilde{Z''^2}$. Thus, the reaction rate for NO formed via the Zeldovich mechanism ($\widetilde{\dot{w}}_{NO,zel}$) in the post flame region is:

$$\widetilde{\dot{w}}_{NO,zel} = \big(1-\widetilde{G}\big)\dot{w}_{NO,zel_{CHEMKIN}}\widetilde{Y_{NO}} \quad (31)$$

Nevertheless, the reaction:

$$N_2 + O_2 \rightleftharpoons 2NO \quad (32)$$

is considered to never be far from equilibrium. Therefore, the rate of formation $\dot{w}_{NO,zel_{CHEMKIN}}$ of NO in the post flame region is constant and independant upon the NO mass fraction.

Thus, the LES NO governing equation is:

$$\frac{\partial \overline{\rho}\widetilde{Y}_{NO}}{\partial t} + \frac{\partial}{\partial x_i}\Big(\overline{\rho}\widetilde{u}_i\widetilde{Y}_{NO}\Big) = \frac{\partial}{\partial x_i}\Big((D+D_T)\overline{\rho}\frac{\partial \widetilde{Y}_{NO}}{\partial x_i}\Big) + \overline{\rho}\Big(S_F \mid \nabla \widetilde{G} \mid Y_{NO,ff} + \big(1-\widetilde{G}\big)\dot{w}_{NO,EQ_{CHEMKIN}}\widetilde{Y_{NO}}\Big) \quad (33)$$

4 Numerical Approach

The LES equations described above are solved using a finite-volume scheme that is nominally second-order accurate in both space and time. The simulation are performed using a three dimensional (3D) as well as a axisymmetric (2D) computational grid. Details of the combustor geometry and the numerical approaches are summarized below.

4.1 The DOE-HAT Geometry

The geometry of the DOE-HAT combustor is shown in figure 1a). In this combustor, the premixed mixture enters the combustor in a swirling manner through a circular slot. The flame is stabilized by the recirculation in the base of the dump and also by the recirculation created by the center body. Figures 1(b) and (c) show respectively, the computational domain and the characteristic grid distribution.

The length of the combustion chamber is 0.6 m, its radius is 0.053 m and the inlet is located between 0.0173 m and 0.0314 m from the centerline. The length of the combustor is chosen so that the emissions predictions (which is only available at 0.381 m from the dump plane) can be computed and compared with data.

The inflow characteristics are chosen as given in the earlier DOE-HAT experiment: the fuel is methane (CH_4) and the reactants enter the combustor with a temperature of 700 K, a pressure of 1.378 MPa., and a mean inflow velocity of 68.6 m/s. The flow is swirling and the swirl number is 0.6. The Reynolds number based on the inlet velocity and the diameter of the centerbody is 120,000. A random turbulent field is added to the inflow mean velocity and a subgrid turbulence intensity of around 7 percent is used to specify the incoming subgrid kinetic energy. Characteristic based inflow and outflow boundary conditions[16] are employed for all the reported simulations.

4.2 3D Grid Topology

In order to resolve shear layer and flame features without being restricted by the cylindrical grid restriction at the centerline, a two-grid approach is employed in this study. The region near the centerline is resolved using a rectangular grid whereas a cylindrical grid is

used elsewhere. Second-order interpolation between the two grid is employed to transfer information back and forth. This two-grid approach is shown in Fig. 2. For the current combustor, all the combustion process occur in regions far from the centerline and the two-grid approach effectively eliminates the centerline time restriction without impacting the physics of interest. Studies were conducted by varying the grid resolution and the size of the inner grid to ensure smooth continuity between the solution in the two grids and also to ensure grid independence is achieved for the resolved scales. The grid resolution used for all the studies reported here is 200x81x101 for the cylindrical grid and 200x22x22 for the inner cartesian grid. The grid is clustered in the region of high shear to resolve the flame zone.

This numerical algorithm is implemented in parallel using Message-Passing Interface (MPI). The two grids overlap, and so once the MPI operations are completed, the interpolation depends only on the information contained in one grid. In the present application, only a 2D interpolation at each axial location is carried out and seems to suffice. A quantity f at a location (y,z) is determined as a function of the quantity known at a point (y_0,z_0) using this relation:

$$f(y,z) = f(y_0,z_0) + \frac{\partial f}{\partial y}dy + \frac{\partial f}{\partial z}dz + \frac{\partial^2 f}{\partial y^2}dydy + 2\frac{\partial^2 f}{\partial y \partial z}dydz + \frac{\partial^2 f}{\partial z^2}dzdz \quad (34)$$

where, if the y-direction is discretized using the j-index and the z-direction is discretized using the k-index ($f(y,z)$ can then be written as $f_{j,k}$) and if Δy is the grid spacing in the y-direction and Δz is the grid spacing in the z-direction:

$$\frac{\partial f}{\partial y} = \frac{f_{j+1,k} - f_{j-1,k}}{2\Delta y}$$
$$\frac{\partial f}{\partial z} = \frac{f_{j,k+1} - f_{j,k-1}}{2\Delta z}$$
$$\frac{\partial^2 f}{\partial y^2} = \frac{f_{j+1,k} - 2f_{j,k} + f_{j-1,k}}{(\Delta y)^2}$$
$$\frac{\partial^2 f}{\partial z^2} = \frac{f_{j+1,k} - 2f_{j,k} + f_{j-1,k}}{(\Delta z)^2}$$
$$\frac{\partial^2 f}{\partial y \partial z} = \frac{f_{j+1,k+1} - f_{j+1,k-1} - f_{j-1,k+1} + f_{j-1,k-1}}{4\Delta y \Delta z} \quad (35)$$

The grid has to be uniform if this interpolation method is used. Thus, the centerline cartesian grid is uniform and the cylindrical grid is uniform in the vicinity of the centerline. The inaccuracy in the interpolation caused by the curvature of the cylindrical grid is assumed to be negligible at present, but this is an issue that will be revisited later.

This approach has two major advantages. First there is no special treatment at the centerline: this method allow large fluxes of mass, momentum and species through the centerline. Second, the time step of the computation can be increased. Nevertheless, interpolation errors (or inaccuracy) can introduce oscillations. Our studies suggest that to avoid these oscillations, the boundary between two grids should not lie in region of high shear or in regions of high pressure or density spatial gradients.

Computations were carried out entirely in parallel using MPI libraries. The LES solver is highly optimized for scalability on nearly all parallel machines, and achieves a speed of $2.4*10^{-5}$ CPU seconds per time step, per grid point, per processor on Compaq SC40. Multiple flow through times (typically 3-4) are recorded (after the initial transients) to obtain stationary statistics. Typically, for the grid noted above approximately 16 single-processor hours are needed for a single flow through time period. Thus, a complete simulation with reliable statistics will require around 2700 single processor hours. Using 56 processors, this reduces to 50 wall clock hours.

4.3 Quasi-3D Approach

The 3D LES described above although feasible at present is still very expensive for parametric studies. One goal of this study was also to determine if a computationally efficient model can also be developed for design level studies. To investigate this, a quasi-3D (Q3D) approach is also developed whereby, the full 3D LES governing equations are solved in axi-symmetric (2D) coordinate system by neglecting all derivatives in the azimuthal direction. With this approach, it is possible to include the effect of swirl (albeit in an axi-symmetric sense). This is critical since swirl is a major component of the inflow. The Q3D model equations are:

$$\frac{\partial \mathbf{U}}{\partial t} + \frac{\partial \mathbf{F}}{\partial x} + \frac{1}{r}\frac{\partial}{\partial r}\Big(r\mathbf{G}\Big) = \frac{\mathbf{H}}{r} \quad (36)$$

Here,

$$\mathbf{U} = \begin{bmatrix} \rho \\ \rho u_x \\ \rho u_r \\ \rho u_\theta \\ \rho E_t \end{bmatrix}$$

$$\mathbf{F} = \begin{bmatrix} \rho u_x \\ \rho u_x u_x - \tau_{xx} + p \\ \rho u_r u_x - \tau_{xr} \\ \rho u_\theta u_x - \tau_{x\theta} \\ (\rho E_t + p)u_x - (u_x\tau_{xx} + u_r\tau_{xr} + u_\theta\tau_{x\theta}) + q_x \end{bmatrix}$$

$$\mathbf{G} = \begin{bmatrix} \rho u_r \\ \rho + u_x u_r - \tau_{xr} \\ \rho u_r u_r - \tau_{rr} + p \\ \rho u_\theta u_r - \tau_{r\theta} \\ (\rho E_t + p)u_r - (u_x\tau_{rx} + u_r\tau_{rr} + u_\theta\tau_{r\theta}) + q_x \end{bmatrix}$$

$$\mathbf{H} = \begin{bmatrix} 0 \\ 0 \\ \rho u_\theta u_\theta - \tau_{\theta\theta} + P \\ \tau_{r\theta} - \rho u_r u_\theta \\ 0 \end{bmatrix}$$

Filtered form of these equations are solved for the LES study here. All the closure models are identical to the models used in the full 3D approach except that all azimuthal variations are neglected.

5 Results and Discussion

To simulate the dynamics of combustion and pollutant production as LBO is approached, a range of equivalence ratio from 0.41 to 0.53 conditions is studied. Experiments have shown that the lowest value (Φ=0.41) is close to LBO. Representative results for these simulations are discussed in the following sections.

5.1 Flame and Flow Characteristics

Change in the equivalence ratio directly influences the propagation speed and therefore, impact the flame shape (length) and the sensitivity of the flame to turbulent eddy motion. As the equivalence ratio decreases, the laminar flame speed decreases and thus, the flame length increases. This has a direct influence upon the pollutants formation at the flame front. Furthermore, the flame shape will directly influence the flow characteristics (this is discussed in the next paragraph).

Furthermore, as the laminar flame speed decreases, the flame surface becomes more sensitive to the turbulent motion, or, in other words, the interactions between the flow and the flame increases. This is shown in Figs. 3 (a) and (b). For Φ=0.53 (Fig. 3a) the flame surface is wrinkled primarily by the large vortical structures created at the edge of the inflow pipe whereas for Φ=0.41, the flame shape is also affected by the smaller turbulent structures (Fig. 3b). Since the turbulent flame speed is a function of u'/S_L, small changes in u' have a great impact on the flame propagation speed for a fixed S_L and this influence increases as Φ decreases (because S_L decreases).

Analysis of the LES flow field suggests that three recirculation regions are created due to the combustor geometry and due to the nature of the flow. These regions are shown schematically in Fig. 4. The first one is created downstream of the bluff body and is attached to the bluff body (Attached Inner Recirculation Region or AIRR). The second one is located further downstream (at a distance D_R from the dump plane) in the vicinity of the centerline and is due to the swirling of the flow. This recirculation region is detached from the bluff body (Detached Inner Recirculation Region or DIRR) and is related to the vortex breakdown phenomenon observed in highly swirling flow.[17] The third recirculating zone is at the base of the dump plane (Attached Outer Recirculation Region or AORR). Length and location of these different recirculation regions for the simulations are summarized in the Table 1.

Equivalence ratio	AIRR length	DIRR length	DR	AORR length
0.53	22	-	-	78
0.45	21	55	63	78
0.41	-	100	30	67

Table 1 Characteristics of the three recirculation regions in the DOE-HAT combustor. Scale is in mm

The shape of the premixed flame and its stability is determined by the presence or the lack of these recirculation zones (see Fig. 4). These recirculation zones are dynamic features that changes not only due to the change in the equivalence ratio but also due to the associated dynamics in the flow field. For Φ>0.5, the flame is short and hot, and the heat release (and the associated thermal expansion) is large. As a result, no DIRR is created but with decrease in the equivalence ratio, a DIRR is created since thermal expansion effect on the flow is reduced. The size (length) of this DIRR increases with decrease in Φ. The size of the DIRR also influences the size and/or the existence of the AIRR and AORR. Decrease in Φ increases the length of the DIRR and moves its leading edge closer to the combustor dump plane. This effect eliminates AIRR downstream of the center body. The AORR is only marginally effected by changes in equivalence ratio.

5.2 Emissions prediction

Emissions prediction from the numerical study are presented on Table 2. The CO and NO mean emission (in ppm), as well as the normalized RMS values of the pollutants mass fraction fluctuations.

Equivalence ratio	CO	CO_{RMS} (percent)	NO	NO_{RMS} (percent)
0.53	10.6	0.00	5.40	1.30
0.45	1.7	0.05	1.14	0.50
0.41	25.6	21.5	0.55	0.50

Table 2 Predicted mean CO and NO emissions (in ppm with 15 percent excess O_2) and the normalized RMS ($Y_{RMS}/\overline{Y}$) of their fluctuations (in percentage). Data reported at the location of the experimental emission probe.

The implication of the observed trend as function of equivalence ratio is discussed in the following sections.

5.3 CO emission

The physics that impact CO emission is investigated in detail by addressing the contribution of the aforementioned three mechanisms of CO production.

5.3.1 Source(s) of CO production

Since CO emission in the combustor is due to a combination of different processes (which do not occur at the same location) it is necessary to investigate the relative contribution of these mechanisms to the overall CO emission. This comparison is shown in Fig. 5. It can be seen that the CO emission due to CO_2 dissociation is decreasing with the equivalence ratio. This is due to the fact that, as the equivalence ratio decreases, the temperature of the burnt product decreases and thus, the equilibrium of the reaction mechanism (described by Eq. 24) shifts to the left.

On the other hand, the CO emission when the CO_2 dissociation is not taken into account increases as the equivalence ratio decreases. This is the combined effect of two mechanisms: CO production across the flame and CO oxidation in the post flame region. These results suggest a question: is the increase in CO emission with decrease in Φ due to more CO formation at the flame front or due to a lower oxidation rate? In Fig. 6 the average CO mass fraction is plotted against the axial distance from the dump plane for different Φ. The initial increase in CO mass fraction is due to the CO formation at the flame front. Beyond the flame, CO mass fraction decreases due to CO oxidation. This mass fraction decreases till the equilibrium (Eq. 24) is reached.

Figure 5 also shows that CO production at the flame increases with decrease in Φ. Since CO formation per unit area at the flame front decreases with decrease in the equivalence ratio, the observed increase in CO at the flame front is explained by an increase in the flame area. The flame surface area increases as Φ is reduced since u'/S_L increases with decrease in S_L. Furthermore, at lower equivalence ratio, the product temperature is lower and thus, the CO oxidation rate is also lower.

5.3.2 Comparison with experiments

Numerical results are compared with experimental data in Fig. 7. Very good agreement is observed at all simulated conditions (both full 3D and Q3D). We focus here primarily on the 3D results and will address the Q3D results later. CO emission shows a minima as a function of equivalence ratio in excellent agreement with data. A critical equivalence ratio is defined Φ_{CR} (in the present case, $\Phi_{CR} = 0.44$) for which CO emission is at a minimum. When $\Phi > \Phi_{CR}$, the total amount of CO produced at the flame front will be oxidized before reaching the emission probe. Thus, the measured emission will be determined by the equilibrium between CO_2 dissociation and CO oxidation. The mass fraction of CO at equilibrium computed using CHEMKIN is thus, a good approximation. This is shown in Fig. 8 where the CO at equilibrium and the experimental emission data are plotted. For $\Phi > \Phi_{CR}$, CO computed by CHEMKIN agree very well with measurements. Note that, over-prediction occurs at higher values of Φ which suggests that equilibrium CO production is not sufficient to explain CO emission at high Φ. This is an issue that will be addressed in the future.

When $\Phi < \Phi_{CR}$, the amount of CO at equilibrium is negligible and thus, CO emission is determined by the balance between CO production at the flame front and by CO oxidation in the post flame region. With decrease in Φ there is more production at the flame front and less oxidation due to lower flame temperature. Therefore, CO mass fraction measured at the emission probe increases when the equivalence ratio decreases. This phenomena has been called kinetic CO by Lefebvre.[18]

5.3.3 Influence of combustion chamber design

Note that, for a given geometry and operating conditions, Φ_{CR} depends upon the location of the emission probe since Φ_{CR} increases when the probe is moved closer to the dump plane and vice-versa. A well-designed combustion chamber should allow for the complete oxidation of CO formed at the flame front. Therefore, a relation between the length required for Eq. 24 to reach equilibrium and the equivalence ratio can be determined. This length is plotted against the equivalence ratio in Fig. 9. The (optimal) minimum CO emission (i.e., the CO equilibrium value) is also plotted on this figure. As the equivalence ratio decreases from 0.7 to 0.5, the value of CO at equilibrium drastically decreases but the length required to reach this value only increases slightly. However, for $\Phi < 0.5$ CO emission decreases further relatively slowly while the combustion length required to reach this value dramatically increases. This has important design implications since although lower CO emission can be achieved by using very lean mixtures, the combustion chamber length can become prohibitively long. Therefore, a good design will have to balance the emission requirements with the geometry constraints. For the DOE-HAT combustor under the test conditions simulated here, an operating equivalence ratio around 0.5 ensures low CO emission (around 4 ppm) while having a relatively small length (approximately 15 cm).

The oscillations in the equivalence ratio of the incoming reactant feed can therefore, impact CO emission as well. If the combustor length is fixed such that minimum CO emission is reached at the end of the combustor, small fluctuations in the equivalence ratio in the feed can lead to a large increase in the overall CO emission of the combustion chamber. Therefore, studies of partially premixed combustion (i.e., with

both spatial and temporal variation in the inlet Φ) is warranted and will be addressed in the near future. Note that the model developed here can be easily used to simulate this effect.

5.3.4 Fluctuation in CO emission near LBO

Figure 10 shows the normalized RMS fluctuation of the CO mass fraction ($Y_{CO,RMS}/\overline{Y_{CO}}$). Only the region downstream of the flame is shown. In general, the fluctuations decrease with axial distance due to turbulent mixing and also due to the "damping" effect of CO consumption via oxidation. The fluctuations tends to zero as equation 24 tends to equilibrium. This is clearly shown in Table 2. When, at the location of the emission probe, Eq. 24 is at equilibrium (Φ=0.53 and Φ=0.45) the RMS of the CO mass fraction fluctuations are negligible. But for Φ=0.41 CO does not reach its equilibrium value at the location of the emission probe and the the fluctuation level is nearly 21 percent. An interesting trend is observed in this figure. The fluctuations are intense closer to the dump plane for high Φ but the magnitude decreases and the location moves further downstream as the equivalence ratio is decreased. On the other hand, the decrease in the RMS with axial distance is larger at high Φ. For low Φ of 0.44 the decrease is RMS is more gradual such that at the location of the emission probe, the lowest Φ shows the largest RMS value.

These results appear to contradict the earlier observation that as the equivalence ratio is reduced, local flame fluctuations increase due to the reduced stability of the flame and therefore, fluctuations in the CO should also increase. However, as shown in Fig. 10, closer to the dump plane CO fluctuation increases with increase in Φ. This phenomenon can be explained by investigating the interaction between the vortical shear flow processes at the dump plane and the flame. For Φ=0.53, the flame is relatively short and thus, the large-scale vortices can directly interact with the flame surface. This effect influences the CO formation at the flame front due to large instantaneous changes in the flame surface area. For Φ=0.41, the flame length is much longer. The vortices still interact with the flame surface but its effect is smaller than when the flame is short. Thus, CO fluctuations are lower near the dump plane for Φ=0.41 when compared to Φ=0.53 case. Further downstream, the fluctuations rapidly decrease for high Φ cases, whereas, for the low equivalence ratio case, the intensity is still significant. Thus, at the emission probe location, the low Φ case should exhibit higher RMS of the fluctuation.

The frequency of the oscillation is also effected by the equivalence ratio. The frequency spectra of the CO mass fraction and the vorticity fluctuations at the dump plane for Φ=0.41 and Φ=0.53 are shown in Figs. 11 and 12, respectively. For a fixed Φ the dominant frequency is same for the vorticity and the CO mass fraction fields indicating a coincidence between the fluid dynamical and chemical processes in the flame zone. The frequency increases with Φ, from 1750 Hz for Φ=0.41 to 2980 Hz for Φ=0.53.

5.3.5 UHC influence upon CO emission

As noted earlier in Section 3.6.2, the unburnt CH_4 released when the flame is quenched due to aerodynamic stretch is not implemented in this study. This unburnt CH_4 or UHC can be an important source of CO in the post flame region since (due to the high temperatures of the post flame region) UHC will not reignite but will be oxidized and form CO. Aerodynamic quenching can be important for low equivalence ratio and can thus, influence the CO emissions. Earlier studies by Held *etal*[4] in a GEAEC LM-6000 combustor showed that post-flame UHC oxidation provides a significant source of CO late in the combustion process. For the present DOE-HAT combustor, however, the good agreement between our LES prediction and experimental data suggests that this mechanism is not that significant, at least at the measurement location. Nevertheless, the UHC effect on CO emission remains an issue to be resolved.

5.4 *NO* Emission

Both thermal and prompt NO emission are modeled in this study and the results are summarized below. Emission prediction from the numerical study are presented on Table 2

5.4.1 Comparison with experiments

Figure 13 shows that the NO emission trend is well predicted by the LES simulations. There is, however, a general under prediction with the under prediction increasing at high Φ. A significant amount of NO formation is due to prompt NO formation at the flame surface. However, analysis of the flow field shows that the NO mass fraction is high in the recirculation zone (AORR) located above the flame. The recirculation zone increases the residence time in the post flame region, and thus, additional NO is produced via the Zeldovitch mechanism.

To evaluate the relative importance of both these mechanisms, NO mass fraction as a function of the axial distance is shown in Fig. 14. For Φ=0.41 and Φ=0.45 the initial increase in NO mass fraction is due to the NO formation at the flame front while in the post-flame region, the Zeldovitch mechanism effect is negligible. For these equivalence ratios, the majority of NO formation is at the flame front and due to the relatively low temperature in the post flame region, no significant amount of NO is produced via the Zeldovitch mechanism. However, for $\Phi = 0.53$ the temperature of the burnt gases is higher and thus, the NO production via the Zeldovitch mechanism becomes significant. As a result, NO mass fraction increases in the post-flame region. This observation is in agreement

earlier studies[19] in lean premixed-prevaporized (LPP) combustor where it was demonstrated that NO does not increase significantly with distance downstream of the combustion zone for equivalence ratio lower than 0.5 and that, above this value, the formation of NO in the post flame region becomes an important mechanism.

For Φ=0.53, the nitrogen oxide mass fraction initially decreases and then increases with a minimum around 70 mm from the dump plane. In the far field, NO level continues to increase for this case and may be because Eq. 32 was far from equilibrium. The increase is due to the post flame thermal NO production via the Zeldovitch mechanism. These results also provide an explanation for the observed differences between the predicted and measured NO emission, and the fact that this difference increases with an increase in Φ. The influence of the Zeldovitch mechanism being negligible for $\Phi < 0.5$, the under prediction is, in this range of equivalence ratio, directly related to the under-prediction of NO formation at the flame front. The formation at the flame front is related to the flame surface and mass fraction of NO formed by a flame element. The fact that CO predictions are in good agreement with the experimental results proves that the flame surface (and its area) is probably well simulated. Thus, the under-prediction of NO formation at the flame front could only be explained by an under-prediction of $Y_{NO,ff}$ by CHEMKIN. Furthermore, the amount of NO produced via the Zeldovitch mechanism being directly proportional to the amount of NO formed at the flame front (the rate of formation via the thermal mechanism is $\dot{w}_{NO,EQ_{CHEMKIN}}\widetilde{Y_{NO}}$), the difference between the predicted and measured NO is expected to increase as the influence of the Zeldovitch mechanism increases, i.e., as the equivalence ratio increases.

Additional possibilities could also exist since for this study the extended Zeldovitch mechanism nor the N_2O-intermediate route were considered.[20]

5.4.2 Fluctuation in NO emission near LBO

The normalized RMS of the NO mixture fraction is plotted against the distance from the dump plane in Fig. 15. The initial mixing region starting at the dump plane and having a length equal to twice the length of the flame is not plotted in this figure. The RMS of the mass fraction fluctuations decreases with the distance from the dump plane for all Φ. For low equivalence ratio (Φ<0.5), the thermal NO mechanism is negligible, and mixing and diffusion processes damp the mass fraction oscillations (similar to their effect on CO). For higher equivalence ratio (Φ>0.5), the additional NO formation in the post-flame region tends to increase the oscillations.

5.5 Quasi-3D Predictions

The Q3D approach attempts to mimic the behavior of the full 3D using an axi-symmetric (2D) model. Since all azimuthal variations are neglected, the effect of non-axisymmetric vortex stretching and breakdown cannot be included. On the other hand, the qualitative influence of swirl on the axial flow (shortening of the recirculation region and the creation of a vortex breakdown region) is reasonably reproduced in the Q3D approach. In the DOE-HAT geometry, the Q3D approach predicts erroneous axial (u) and azimuthal (w) velocity profiles (including magnitude) near the centerline. However, this is of relatively less importance since most of the flame zone is located away from the centerline. Nevertheless, in the Q3D simulations, the over prediction of the axial velocity component at the centerline reduces the combustion chamber residence time. The attached outer recirculation region (AORR) is over predicted with decrease in Φ as summarized in Table 3.

Equivalence Ratio	3D AORR length	Q3D AORR length
0.53	78	72
0.45	78	96
0.41	67	99

Table 3 Length of the AORR as a function of the equivalence ratio. Comparison between the 3D and the Q3D approach. Lengths are in mm.

The sensitivity of the CO and NO emission to the Q3D approximation is addressed in the following.

5.5.1 CO emission

Simulations at the same equivalence ratios as in the full 3D studies were carried using the Q3D model. Good agreement for CO emission with full 3D LES and experimental data ican be seen in Fig. 7. Since for $\Phi > \Phi_{CR}$, CO emission is determined by its equilibrium value (which is obtained from the flamelet library) it is not surprising that both 3D and Q3D results are similar. For $\Phi < \Phi_{CR}$ emission prediction is slightly higher even though the overall trend in CO emission with Φ is well reproduced. This is probably a result of a decrease in residence time in the Q3D simulation compared to the 3D simulation. In the Q3D simulation, no relaxation of the fluid motion is allowed in the circumferential direction and as a result, the flow accelerates at the centerline (section 5.5). This will decrease the total residence time and as a result, there will be less time for the CO produced at the flame front to be oxidized. Thus, CO emission prediction will be higher in the Q3D simulation.

5.5.2 NO emission

Q3D prediction of NO emission is also plotted in Fig. 13. Again, there is a good agreement between full

3D and Q3D results. For $\Phi > 0.5$, the Q3D predictions are slightly lower than the 3D predictions (4.9 ppm v/s 5.4 ppm). This may reflect the effect of a slightly smaller size of the AORR in the Q3D simulation on the thermal NO production in this post flame region (see Table 3). This can also reflect a slightly smaller residence time in the post-flame region with regard to the 3D simulation (This last remark confirms the decrease in residence time observed in the CO emission data). Therefore, the reduction in residence time and the reduction of the AORR size in the Q3D approach explains the slightly lower NO emission predictions of the Q3D approach.

5.5.3 Potential of Q3D approach as a design tool

The main advantage of the Q3D approach is its computational efficiency. In the present study, the typical grid size for the Q3D approach is around 24000 points whereas, over 1.6 million grid points is used for the full 3D LES. Thus, for Q3D the computational cost is trivial ($5.1*10^{-6}$ sec per step per grid point per processor on a Compaq SC40 Machine) and a full simulation can be completed in 1.5 single processor hours on 7 processors. On a Intel Pentium 4 Xeon 2.2 GHz Cluster, it will take only 5 wall clock hours to complete a simulation on 7 processors. Therefore, many simulations can be conducted rapidly, as is required in a design cycle.

The above analysis has shown that in spite of the reduction in dimensionality, the Q3D approach can provide realistic estimate for CO and NO emission as a function of the equivalence ratio. On the other hand, many 3D features such as 3D azimuthal breakdown of structures and any associated effect on pollutant emission are not included in Q3D. For the DOE-HAT combustor studied here these 3D effects appear negligible but this conclusion cannot be generalized for all gas turbine combustors.

On the other hand, the development of both full 3D and quasi-3D models demonstrated here suggest a viable approach to include LES into the design cycle. In this approach, a limited number of full 3D LES is carried out to map out the general trends for a given combustor and then these conditions are repeated using the Q3D approach. Similarities and differences can then identified and quantified. Subsequently, the Q3D model can be used to carry out additional parametric studies keeping the inherent strengths and weaknesses in perspective. Full 3D LES can by used intermittently to re-evaluate the accuracy of the Q3D approach. If necessary, the full 3D LES results can be used to modify the Q3D model to further increases its reliability. This approach may provide a means to carry out design-level parametric study of unsteady dynamics and pollutant formation in new combustor designs for which no experimental data is available. It remains to be seen if such a methodology can be fully established for practical application.

6 Conclusion

In this study, a LES methodology that combines a thin-flame model for flame tracking along with transport models for CO, NO and UHC species is used to predict emission and unsteady dynamics in a full-scale DOE-HAT combustor under experimental conditions. Subgrid closures for the LES model are developed and implemented for this study. Results are obtained using a a full 3D model as well as a quasi-3D model which includes swirl effect (i.e., azimuthal velocity) within an axi-symmetric formulation. The effect of varying the equivalence ratio is studied using both approaches and the results are compared with experimental data for CO and NO emission.

The simulations also show that an increase in flame oscillation (and associated flow oscillation) occurs as the LBO limit is approached. These results are consistent with experimental observations.

Very good agreement with measurements are obtained for both CO and NO over a range of equivalence ratios. This study also allowed us to get a better understanding of the various mechanisms leading to an exponential increase in the CO emission as the lean flammability limit is reached. The dominant mechanism when equivalence ratio is large is the CO equilibrium process but when the equivalence ratio is close to the lean flammability limit, the mechanism controlling the CO emission is the CO production at the flame front.

The prediction of NO emission in this combustor is also reasonable. The contribution of both the prompt mechanism (at the flame front) and the thermal mechanism (in the post-flame regions) is evaluated and analysis suggest that post flame production is only significant for high equivalence ratio. This result is also in good agreement with observations and past studies in LPP systems.

The good agreement with data using the computationally efficient Q3D model suggests an approach, whereby both full 3D and quasi-3D LES models are used together to carry out in a computationally efficient and affordable manner, design level simulations of combustion dynamics and pollutant emission in new combustors for which no data may exist. Such a capability could help reduce the design iterations of future, low emission gas turbine combustors.

7 Acknowledgements

This work was made possible with the support in part by General Electric Aircraft Engine Company and CFD Research Corporation, AL (prime sponsors are Department of Energy and Wright Patterson AFB). Support for some of the computations was provided by DOD HPC Center at ERDC (MS).

References

[1] Bhargava, A., Kendrick, D. W., Colket, M. B., Sowa, W. A., Casleton, K. H., and Maloney, D. J., "Pressure Effects on NOx and CO emission in industrial gas turbines," *Trans. of the ASME*, Vol. 2000-GT-8, 2000.

[2] Held, T. J. and Mongia, H. C., "Application of a Partially Premixed Laminar Flamelet Model to a Low-Emission Gas Turbine Combustor," *ASME-98-GT-217*, 1998.

[3] Held, T. J. and Mongia, H. C., "Emissions Modeling of Gas Turbine Combustors using a Partially-premixed Laminar Flamelet Model," *AIAA-98-3950*, 1998.

[4] Held, T. J., Mueller, M. A., and Mongia, H. C., "A Data-Driven Model for NO_x, CO and UHC Emissions for a Dry Low Emissions Gas Turbine Combustor," *AIAA-2001-3425*, 2001.

[5] Erlebacher, G., Hussaini, M. Y., Speziale, C. G., and Zang, T. A., "Toward the Large-Eddy Simulation of Compressible Turbulent Flows," *Journal of Fluid Mechanics*, Vol. 238, 1992, pp. 155–185.

[6] Kim, W.-W., Menon, S., and Mongia, H. C., "Large-Eddy Simulation of a Gas Turbine Combustor Flow," *Combustion Science and Technology*, Vol. 143, 1999, pp. 25–62.

[7] Smagorinsky, J., "General Circulation Experiments with the Primitive Equations," *Monthly Weather Review*, Vol. 91, No. 3, 1993, pp. 99–164.

[8] Menon, S., Yeung, P.-K., and Kim, W.-W., "Effect of Subgrid Models on the Computed Interscale Energy Transfer in Isotropic Turbulence," *Computers and Fluids*, Vol. 25, No. 2, 1996, pp. 165–180.

[9] Kim, W.-W. and Menon, S., "A new incompressible solver for large-eddy simulations," *International Journal of Numerical Fluid Mechanics*, Vol. 31, 1999, pp. 983–1017.

[10] Kim, W.-W. and Menon, S., "Numerical Simulations of Turbulent Premixed Flames in the Thin-Reaction-Zones Regime," *Combustion Science and Technology*, Vol. 160, 2000, pp. 119–150.

[11] Chakravarthy, V. and Menon, S., "Large-Eddy simulations of turbulent premixed flames in the flamelet regime," *Combustion Science and Technology*, Vol. 162, 2000, pp. 1–48.

[12] Chakravarthy, V. and Menon, S., "Subgrid Modeling of Premixed Flames in the Flamelet Regime," *Flow, Turbulance and Combustion*, Vol. 5, 2000, pp. 23–45.

[13] Kee, J. R., Rupley, F. M., and Miller, J. A., "CHEMKIN-II A Fortran Chemical Kinetics Package for the Analysis of Gas Phase Chemical Kinetics," Tech. Rep. SAND89-8009B, Sandia National Laboratories, 1992.

[14] Peters, N., *Turbulent Combustion*, Cambridge Monographs on Mechanics, 2000.

[15] Pocheau, A., "Scale Invariance in Turbulent Flont Propagation," *Physical Review E*, Vol. 49, 1994, pp. 1109–1122.

[16] Poinsot, T., Veynante, D., and Candel, S., "Quenching processes and premixed turbulent combustion diagrams," *Journal of Fluid Mechanics*, Vol. 228, 1991, pp. 561–606.

[17] Lilley, G., "Swirl Flows in Combustion: A Review," *AIAA Journal*, Vol. 15, No. 8, 1977, pp. 1063–1078.

[18] Lefebvre, A. H., *Gas Turbine Combustion*, Taylor and Francis, 2nd ed., 1999.

[19] Leonard, G. and Correa, S., "NOx Formation in Premixed High Pressure Lean Methane Flames," *Fossil Fuel Combustion Symposium*, 1990, pp. 69–74.

[20] Turns, S. R., *An Introduction to Combustion. Concept and Applications*, Mac Graw Hill, 1999.

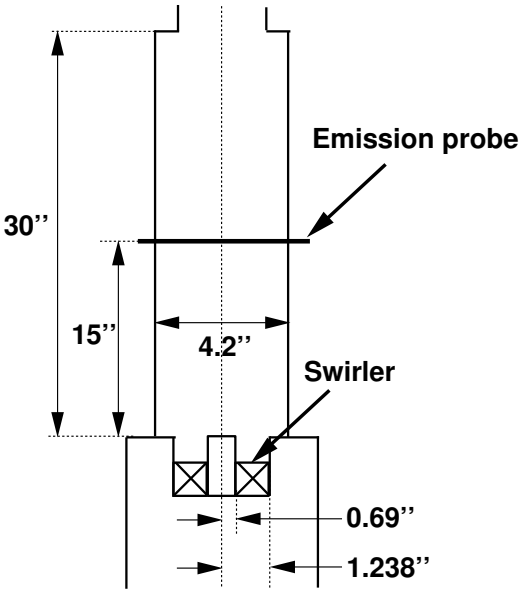

a) Sketch of the DOE-HAT Combustor setup

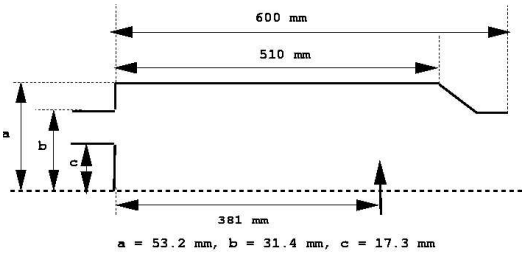

b) Schematic of the DOE-HAT combustor. The location of the emission probe is shown by an arrow.

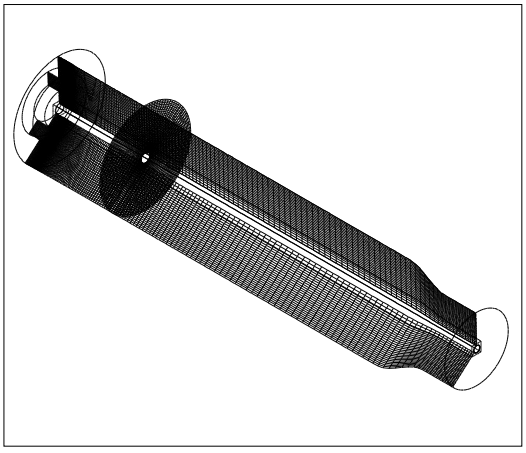

c) General view of the 3D computational domain

Fig. 1 Geometry and dimensions of the DOE-HAT combustor and the computational domain

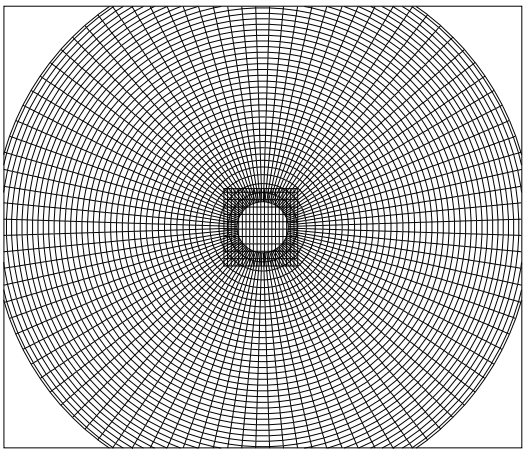

Fig. 2 Front view of the grid mesh showing the cartesian grid (inside) and the cylindrical grid (outside).

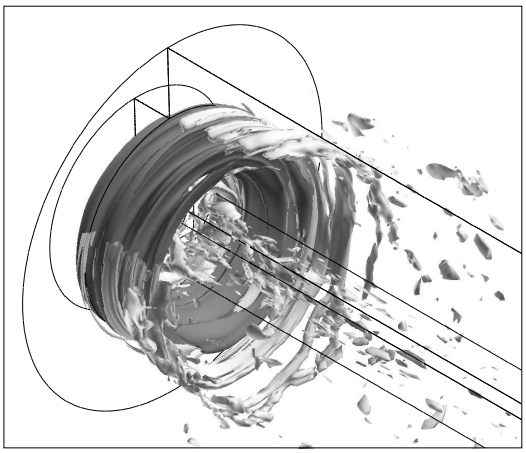

a) Flame surface for $\Phi = 0.53$ (dark) and azymuthal vorticity isosurface (hell) - $w_\theta = 15{,}000\ s^{-1}$

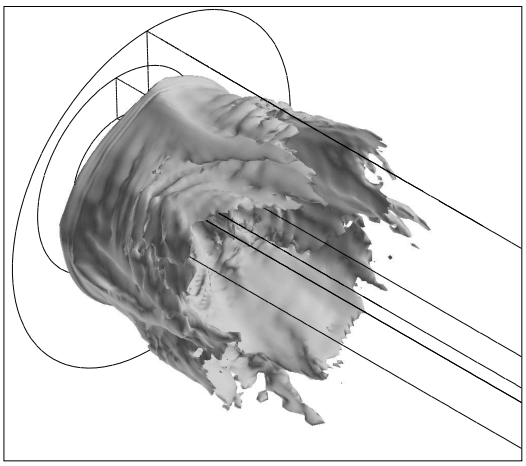

b) Flame surface for $\Phi = 0.41$

Fig. 3 Flame surfaces (G=0.5). The influence of azimuthal vortices upon the flame structure is showed for $\Phi = 0.53$.

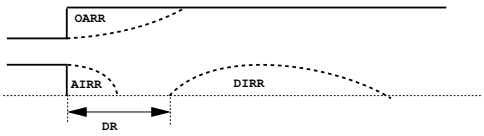

Fig. 4 Recirculation regions existing in the DOE-HAT combustor. OARR: Outter Attached Recirculation Region, AIRR: Attached Inner Recirculation Region, DIRR: Detached Inner Recirculation Region, DR: Distance from the dump plane to the DIRR.

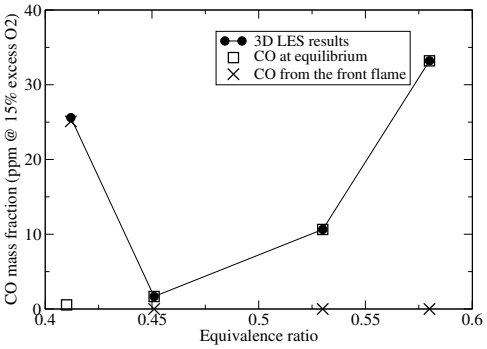

Fig. 5 Influence of the different CO mechanism on the overall CO emission. Numerical results, CO mass fraction at equilibrium and CO mass fraction due to prompt mechanism and oxidation mechanims are plotted. Results are shown at the location of the emission probe

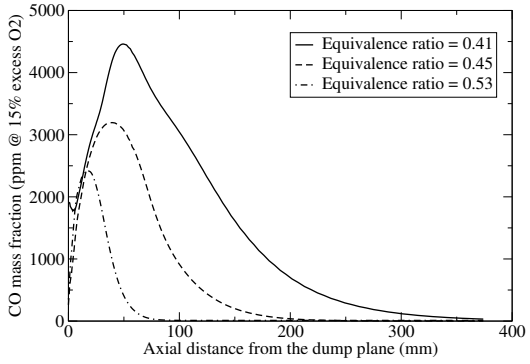

Fig. 6 CO mass fraction (in ppm @ 15 percent excess O_2) vs. axial distance from the dump plane for different equivalence ratio.

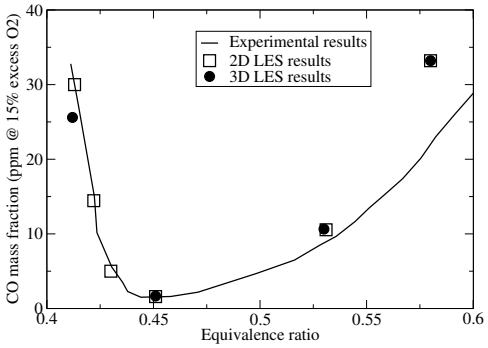

Fig. 7 CO mass fraction (in ppm @ 15 percent excess O_2) from experimental data, 3D and Q3D computations as a function of the equivalence ratio.

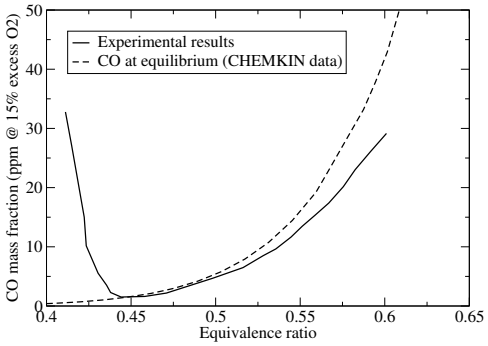

Fig. 8 CO mass fraction (in ppm @ 15 percent excess O_2) equilibrium value compared with experimental CO emission measurements. For Φ>0.44, the CO equilibrium value controls the emission.

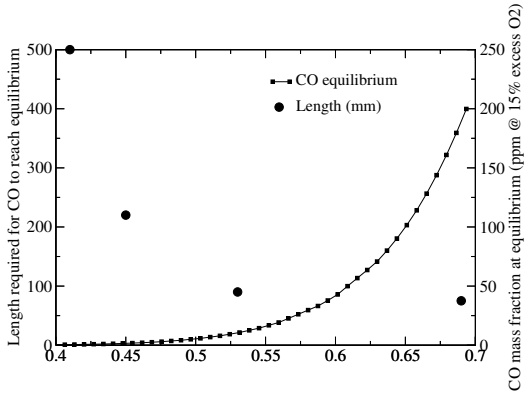

Fig. 9 Combustion chamber length required to reach the CO equilibrium value and CO equilibrium value as a function of the equivalence ratio

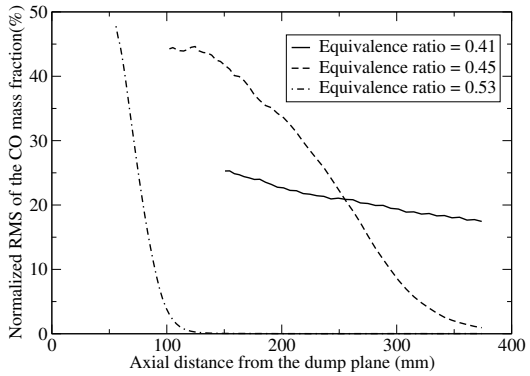

Fig. 10 Normalized CO mass fraction fluctuations RMS ($Y_{CO,RMS}/\overline{Y_{CO}}$) as a function of the axial distance from the dump plane for different equivalence ratio

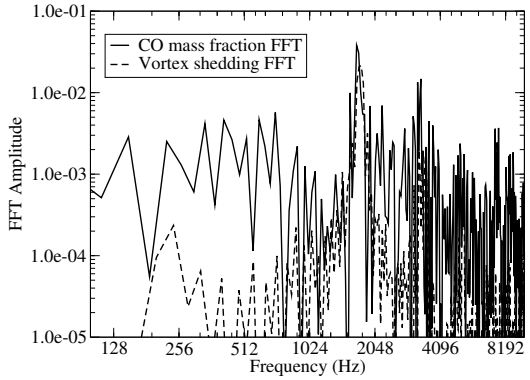

Fig. 11 *CO* **mass fraction and vorticty fluctuation spectra for Φ=0.41**

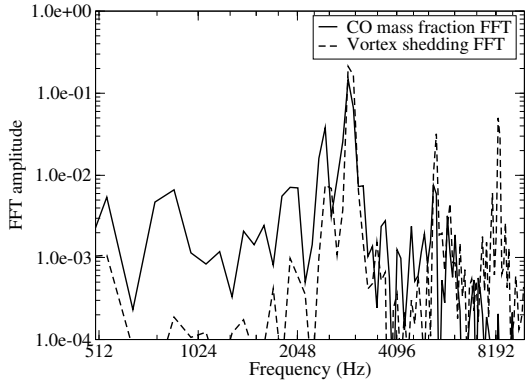

Fig. 12 *CO* **mass fraction and vorticity fluctuation spectra for Φ=0.53**

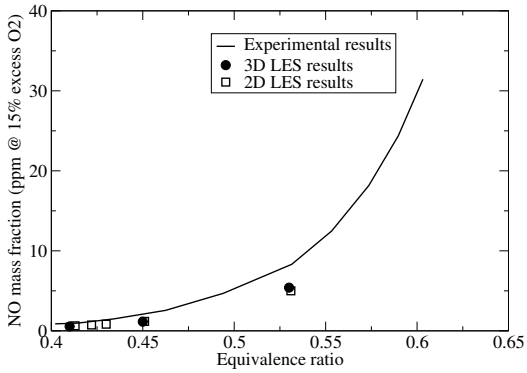

Fig. 13 NO mass fraction (in ppm @ 15 percent excess O_2) from experimental data, 3D and Q3D computations vs. equivalence ratio.

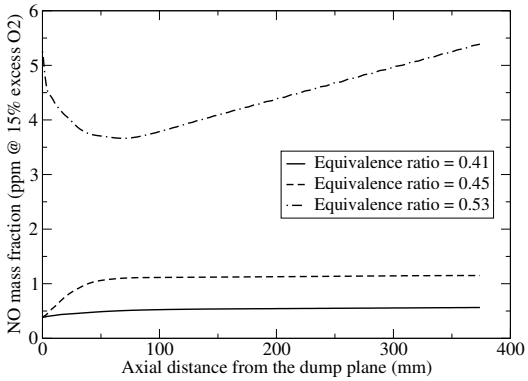

Fig. 14 NO mass fraction (in ppm @ 15 percent excess O_2) as a function of the axial distance from the dump plane for different equivalence ratio.

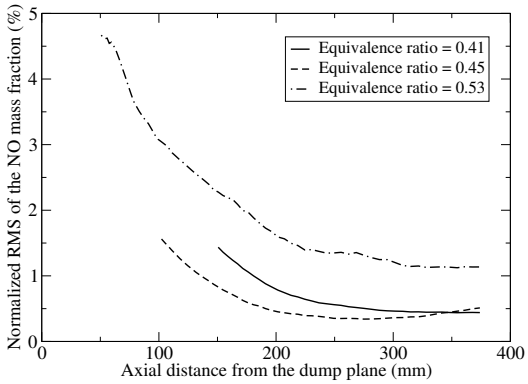

Fig. 15 Normalized NO mass fraction fluctuations RMS ($Y_{NO,RMS}/\overline{Y_{NO}}$) as a function of the axial distance from the dump plane for different equivalence ratio.